AIAA JOURNAL
Vol. 44, No. 2, February 2006

Unsteady Simulation of a Synthetic Jet in a Crossflow

Julien Dandois* and Eric Garnier†
ONERA, 92322 Châtillon Cedex, France
and
Pierre Sagaut‡
Université Pierre et Marie Curie, 75252 Paris Cedex 5, France

The purpose is to address some issues concerning the computation of the interaction of a synthetic jet with a turbulent boundary layer. The main question arising is, What accuracy can be expected according to the grid resolution and the turbulence model? With a view of comparison, large-eddy simulation (LES) and unsteady Reynolds-averaged Navier–Stokes (URANS) simulations on three grids are presented. The computational configuration corresponds to the case number 2 of the CFD Validation Workshop of Synthetic Jets (CFDVAL2004) held in March 2004 at the NASA Langley Research Center. The incoming flow is a canonical turbulent boundary layer with a momentum-thickness-based Reynolds number Re_θ equal to 4275. The synthetic jet has a Strouhal number based on the jet diameter and the jet velocity of 0.019. The ratio of the jet maximum velocity to the crossflow one is 1.45. The ratio of the jet diameter to the boundary-layer thickness is one-third. The whole cavity is computed, and an alternating blowing/suction condition is imposed on its lower surface to model the diaphragm displacement. The effects of mesh size, time step, turbulence modeling, and boundary conditions have been carefully documented. The variation of these numerical parameters has only a moderate influence on the computation/experiment agreement, which remains very satisfactory in all cases. For example, even the URANS computation on the coarsest grid with only 220,000 cells is able to reproduce the synthetic jet dynamics and provides good results for the mean and phase-averaged velocity profiles. Nevertheless, in this case turbulence stresses are not computed with sufficient accuracy, and a LES with realistic inflow boundary conditions on a fine mesh is necessary to recover the right stresses behavior.

Nomenclature

d	=	orifice diameter
f	=	actuator frequency
Re_θ	=	momentum thickness Reynolds number $U_\infty.\theta/\nu$
U_j	=	jet velocity amplitude
U_∞	=	crossflow velocity
u	=	streamwise velocity
v	=	spanwise velocity
w	=	vertical velocity
x	=	streamwise coordinate
y	=	spanwise coordinate
z	=	vertical coordinate
δ	=	boundary-layer thickness
θ	=	boundary-layer momentum thickness
ω_x	=	longitudinal vorticity

I. Introduction

A LOT of attention has been paid in the literature to crossflow jets because they are used in many practical applications: film cooling in turbine, fuel injection, pollutants emission, etc. The objectives of each application are different: for film cooling, the goal is to keep the jet attached to the wall,[1,2] whereas for fuel injection the aim is to enhance the mixing.[3] The formation mechanism of the counter-rotating vortex pair downstream of the jet has been studied extensively and has given rise to many debates.[4–9] All of these studies have focused on steady jet. Periodic excitation of the jet has also received some interest initially for the study of vortex rings formation[10] or for the penetration and the mixing enhancement of jets in crossflows.[3,11,12]

Synthetic jets are actuators that have been proven to effectively control separation,[13] enhance mixing,[14] and vector thrust.[15] The advantage of synthetic jets with respect to steady blowing or suction is that they need less momentum by one or two orders of magnitude to achieve equivalent effects.[13] They also do not require a complex plumbing system because the momentum expulsion is only caused by the periodic motion of a diaphragm or a piston on the lower wall of a cavity.

The interaction of a synthetic jet in crossflow has been studied experimentally by Schaeffler,[16] Smith,[17] Zaman and Milanovic,[18,19] Gordon and Soria,[20] Narayanan et al.,[21] and numerically by Cui et al.,[22] Mittal et al.,[23] and Lee and Goldstein.[24] The latter paper presents a very low-Reynolds-number direct numerical simulation (DNS) aiming at demonstrating the control of longitudinal boundary-layer vortices by synthetic jet, whereas the two first are based on two-dimensional unsteady Reynolds-averaged Navier–Stokes (URANS) computations. Furthermore, an important numerical contribution to the study of synthetic jet without crossflow was the DNS of Rizzetta et al.,[25] which has demonstrated the need to take the cavity into account.

Up to now, the interaction of a circular synthetic jet with a turbulent boundary layer has not been studied with much attention using highly accurate methods such as large-eddy simulation (LES) or DNS. These methods are supposed to be of particular interest for the physical understanding of such flows. It is well known that synthetic jets energize the low-momentum region of the boundary layer during the blowing and remove it in the suction phase, but the flow structure resulting from the interaction of a jet with a boundary layer remains to be fully understood.

Before addressing the physical understanding of synthetic jets, it is needed to consider the following numerical issues: What kind of mesh resolution is necessary to represent the jet? Which kind of modeling should be used (URANS, LES, DNS)? Which boundary

Received 16 September 2004; revision received 4 April 2005; accepted for publication 21 April 2005.

*Ph.D. Student, Applied Aerodynamic Department, B.P. 72, 29 avenue de la division Leclerc.

†Research Engineer, Applied Aerodynamic Department, B.P. 72, 29 avenue de la division Leclerc; egarnier@onera.fr.

‡Professor, Laboratoire de Modélisation pour la Mécanique, Boite 162, 4 Place Jussieu; also Consulting Scientist, CFD and Aeroacoustics Department, ONERA, 92322 Châtillon Cedex, France.

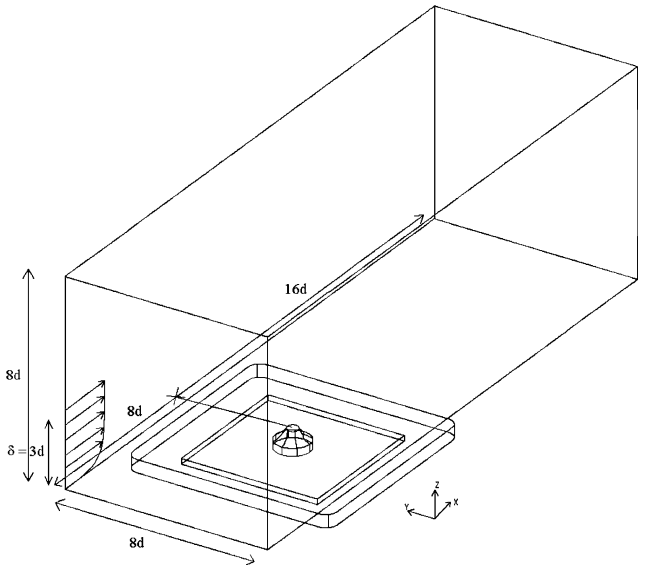

Fig. 1 Flow configuration sketch and computational domain dimensions.

condition to represent the diaphragm? What time step? This methodological paper aims at answering these questions. This work was part of the CFD Validation Workshop of Synthetic Jets and Turbulent Separation Control (CFDVAL2004[§]) which was organized by the NASA Langley Research Center in March 2004 to coordinate a scientific community effort on the computation of synthetic jets. Three cases were investigated: a synthetic jet in quiescent air, into a turbulent boundary layer, and over a hump model. Experimental data for the validation of computational-fluid-dynamics codes were provided for these three configurations. For the second case, these data are from Schaeffler and Jenkins.[26] The computation of a circular synthetic jet in a crossflow is the most challenging of the three cases because it is the only one that cannot be treated in a two-dimensional framework.

This paper is organized as follows. First, the flow configuration is given. Then, the numerical method is presented. In the third part, the influence of the time step, the actuator boundary condition, the mesh size, and the turbulence model is explored, and results are compared to the experimental data of Schaeffler and Jenkins.[26]

II. Flow Configuration

Figure 1 presents the flow configuration and the size of the computational domain. The coordinate system is the following: x is oriented in the streamwise direction, y in the spanwise direction, and z is normal to the wall. The axis origin is located at the center of the orifice.

The flow parameters are those of the experiment of Schaeffler and Jenkins.[26] The Mach number of the inflow boundary layer is 0.1. This corresponds to a freestream velocity U_∞ of 34.6 $\mathrm{m}\cdot\mathrm{s}^{-1}$. The maximum output velocity of the jet is 50 $\mathrm{m}\cdot\mathrm{s}^{-1}$, and its operating frequency is fixed to 150 Hz. The jet diameter d is 6.35 mm, which is one-third of the local boundary-layer thickness δ. Its Strouhal number based on the diameter and the maximum output velocity is 0.019. The Reynolds number based on the momentum thickness is $Re_\theta = 4275$ with $\theta = 2$ mm. The ratio of the jet maximum velocity to the boundary layer one is 1.45.

In all of the following, the results are nondimensionalized by the crossflow velocity U_∞. The x and y coordinates are nondimensionalized by d and z by δ.

III. Numerical Method

The unsteady, three-dimensional, compressible Navier–Stokes equations are solved using two different types of turbulence modeling. First, the URANS and the Spalart–Allmaras model are presented. Then, the large-eddy-simulation equations and the subgrid-scale model will be described.

A. URANS Modeling

The synthetic jet in a crossflow has the particularity of having a well-defined forcing frequency. This problem can then be treated with the decomposition proposed by Hussain and Reynolds,[27] where any fluctuating quantity $f(\boldsymbol{x}, t)$ is written as

$$f = \bar{f} + \tilde{f} + f' = \langle f \rangle_\phi + f' \tag{1}$$

$\bar{f}$ is the global mean value, $\tilde{f}$ the periodic component, and f' the random component (turbulence). Moreover, we can define the phase-averaged value of f as $\langle f \rangle_\phi = \bar{f} + \tilde{f}$. The phase-average operator is defined as

$$\langle f \rangle_{\phi_n} = \frac{1}{m_T} \sum_{m=1}^{m_T} \frac{1}{\Delta\Phi} \int_{(n-\frac{1}{2})\Delta\Phi + (m-1)T}^{(n+\frac{1}{2})\Delta\Phi + (m-1)T} f(t)\,\mathrm{d}t \tag{2}$$

with $\Delta\Phi = T/n_\Phi$, n_Φ is the number of phases in a period, n is the phase number, and m_T is the number of periods of phase averaging. The mean value of the fluctuation is $f - \bar{f} = \tilde{f} + f'$, where $f' \ll \tilde{f}$. The mean turbulent stresses are therefore mainly caused by the periodic component. The phase-averaged fluctuation is defined as $f - \langle f \rangle_\phi = f'$. For the phase-averaged turbulent stresses, the turbulence model has to be added to take into account the effect of the high frequencies on the flow.

In this study, the Spalart–Allmaras (SA) model[28] has been used in URANS mode. The trip terms were not implemented in the code. The transport equation for the variable $\tilde{\nu}$ used here has not exactly the original form of the model, but it is rather a possible extension to compressible flows.[29] To ensure a nonnegative eddy viscosity $\tilde{\nu}$, the linearization of the transport equation follows the SA turbulence approach.[28] An implicit operator is constructed following Baldwin and Barth[30] to obtain $\tilde{\nu} \geq 0$ at all grid points.

B. Large-Eddy Simulation

Because of the Reynolds number of the flow configuration ($Re_\theta = 4275$), the flow is turbulent, and a wide range of scales are present. The idea of LES is to limit the computational cost by solving only the largest scales of the flow while modeling the smallest. Any flow variable ϕ can be written as $\phi = \bar{\phi} + \phi'$, where $\bar{\phi}$ represents the resolved part of ϕ and ϕ' its subgrid part. Mathematically, the filtering is expressed in physical space as a convolution product. In practice, the filtering operator is classically defined as a convolution product on the grid cell, and for a finite volume discretization $\bar{\phi}$ is simply a volumic average over the computational cell. Further details concerning this approach can be found in the Ref. 31.

In our code FLU3M, the Navier–Stokes equations are solved in conservative form. The full system of equation is written following Vreman.[32] The effects of subfilter scales on resolved ones are taken into account via a subgrid-scale (SGS) model. The subgrid-scale tensor τ_{SGS} is modeled via a Boussinesq-like approximation, which requires a model for the SGS viscosity. In this study, the selective mixed-scale model developed by Sagaut [31] has been used. The expression of the subgrid viscosity is

$$\nu_t = C_m(\alpha)|\tilde{S}(\boldsymbol{x}, t)|^\alpha \left[q_c^2(\boldsymbol{x}, t)\right]^{(1-\alpha)/2} \Delta^{1+\alpha} f_s \tag{3}$$

where $C_m = 0.1$, $\alpha = 0.5$, f_s is a selection function, which tests the tridimensionality of the flow (see Ref. 33 for more details), and q_c is the kinetic energy of the smallest resolved scales, which is evaluated by means of a test filter with a cutoff $\Delta = \sqrt{6}\Delta$, where Δ is the cubic root of the cell volume:

$$q_c^2(\boldsymbol{x}, t) = \tfrac{1}{2}(u - \breve{u})(u - \breve{u})$$

where

$$\breve{u}_i = (u_{i-1} + 2u_i + u_{i+1})/4 \tag{4}$$

[§]Data available online at http://cfdval2004.larc.nasa.gov [cited 2004].

C. Numerical Scheme

The FLU3M solver, developed by ONERA, is based on a cell-centered finite volume technique and structured multiblock meshes. For efficiency, an implicit time integration is employed to deal with the very small grid size encountered near the walls. The time integration is carried out by using Gear's backward scheme, which is second-order accurate. Because of the implicit terms, a nonlinear system has to be solved. This is achieved by means of an approximate Newton method. At each iteration of this inner process, the inversion of the linear system relies on lower–upper symmetric Gauss–Seidel implicit method. More details about these numerical points are available in Ref. 34. The spatial scheme is the one proposed by Mary and Sagaut.[35] It is based on the AUSM + (P) (Ref. 36) scheme whose dissipation is proportional to the local fluid velocity, and so it is well adapted to low-Mach-number simulations. Concerning the viscous fluxes, a second-order-accurate centered scheme is used.

D. Mesh and Boundary Conditions

Three different block-structured meshes have been used. The grid is composed of 14 domains. The physical size of the computational domain is the same as the grid posted on the workshop website[§]: the streamwise length is 152.4 mm or 24d (8d upstream and 16d downstream); the spanwise and vertical length are both equal to 76 mm or approximately 12d.

The cells repartition in each part of the domain (cavity, orifice, external field) is shown in Table 1. The fine grid M1 has been designed for the transport of realistic inflow boundary-layer structures, whereas the other two meshes are only built to study the number of mesh points necessary in the jet. The fine grid M1 has 8.9×10^6 cells, the intermediate grid M2 1.7×10^6, and the coarse grid M3 0.22×10^6 cells. For the generation of realistic inflow conditions, an additional domain with about 2×10^5 cells is added to the M1 grid. Table 2 provides the mesh size and grid spacings in the central refined zone before the jet. For the M1 grid, the grid spacings given in Table 2 are valid only in the three-jet-diameter-width refined zone centered on $y = 0$. In this zone, the grid spacings are constant in the wall-parallel directions. In the vertical direction, a grid stretching lower than 10% is applied. For the M1 grid, there are 436 points on the jet circumference; for the M2 grid, there are 172 points and for the M3 grid, 66 points. Figures 2 and 3 present a view of the grid in the x–y and x–z planes, respectively, for the intermediate grid M2.

The boundary conditions are shown in Fig. 4. On the whole cavity's bottom surface, a blowing/suction condition with a top-hat distribution, which varies sinusoidally in time, is implemented to simulate the diaphragm motion: $u(x, t) = U_0 * \cos(2\pi f t)$ with $U_0 = 0.273$ m $\cdot$ s^{-1} and $f = 150$ Hz. U_0 has been calculated by using, on the one hand, the sections ratio between the orifice and the cavity bottom surface and, on the other hand, a target maximum output velocity of 50 m $\cdot$ s^{-1}.

Table 1 Cell repartition

Mesh designation	External field	Orifice	Cavity	Total
Fine with inflow domain (M1 + F)	7.5×10^6	1.3×10^6	279,000	9.1×10^6
Fine (M1)	7.31×10^6	1.3×10^6	279,000	8.9×10^6
Intermediate (M2)	1.25×10^6	263,000	98,000	1.7×10^6
Coarse (M3)	185,000	26,500	10,800	222,600

Table 2 Cell size

Mesh designation	Δx, mm	Δy, mm	$\Delta z_{\min}$, mm	Δx^+	Δy^+	Δz^+
Fine (M1)	0.581	0.222	0.012	48	18	1
Intermediary (M2)	1.28	1.11	0.036	106	92	3
Coarse (M3)	2.56	3.71	0.072	213	309	6

Table 3 Actuator boundary condition and time-step value study

Case designation	Time step, μs	Number of subiterations	Surface of the boundary condition	U_0, m $\cdot$ s^{-1}
A	1	8	Piston + diaphragm	0.273
B	0.5	8	Piston + diaphragm	0.273
C	1	8	Piston	0.725

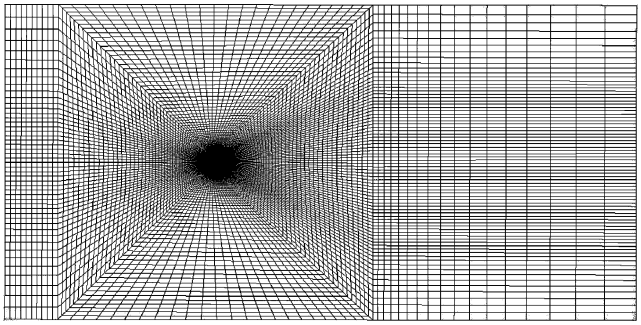

Fig. 2 X–Y view of the M2 grid.

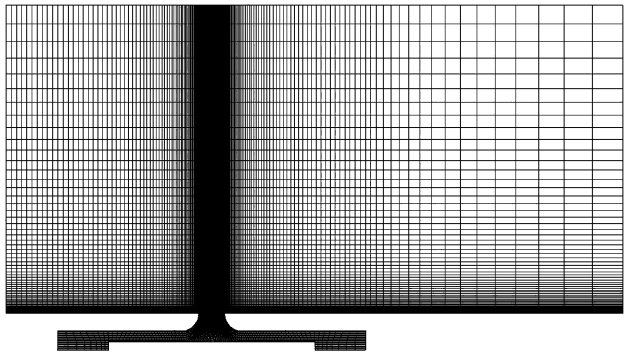

Fig. 3 X–Z view of the M2 grid.

IV. Results and Discussion

A. Preliminary Study of Some Numerical Parameters

A preliminary study of the influence of the actuator boundary condition and time step has been performed on the M2 grid. Table 3 shows the values of different varying parameters.

Case A is the reference. In case B, the time step is reduced from 1 to 0.5 μs. For the first two cases, the blowing/suction condition is applied both on the piston and diaphragm. For case C, instead of using a sinusoidal function, a polynomial fit of driver displacement derivative has been used as a velocity law. In that case, the blowing/suction condition is applied only on the piston.

The number of subiterations of the implicit time scheme has been chosen in order to achieve at least a one-order decrease of the residues. This empirical criterion comes from our experience with FLU3M.[35,37–39] At this low Mach number ($M = 0, 1$), eight subiterations are required to match our criterion and will be used in the following.

Figure 5 shows the phase-averaged longitudinal distribution of the vertical velocity for four different phases. (The phase duration is 10 deg like in the experimental results.) It demonstrates that the solution is not appreciably dependent on the time-step value. The maximum difference between cases A and B is 6% for the phase 205 deg. Consequently, for the computations presented in the next section the time step was fixed to 1 μs for the M2 grid. Furthermore, although the actuator boundary condition of case C is more realistic, the results are less accurate than those of case A in particular for the phase 205 deg, and the simplest boundary conditions have been selected.

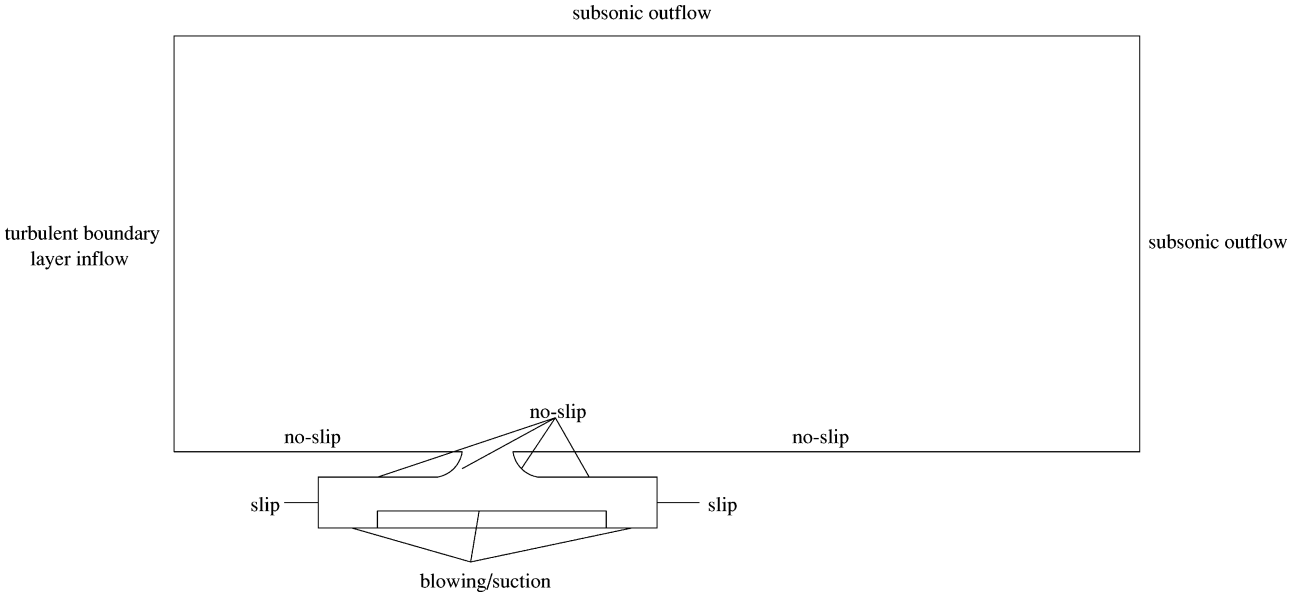

Fig. 4 Boundary conditions.

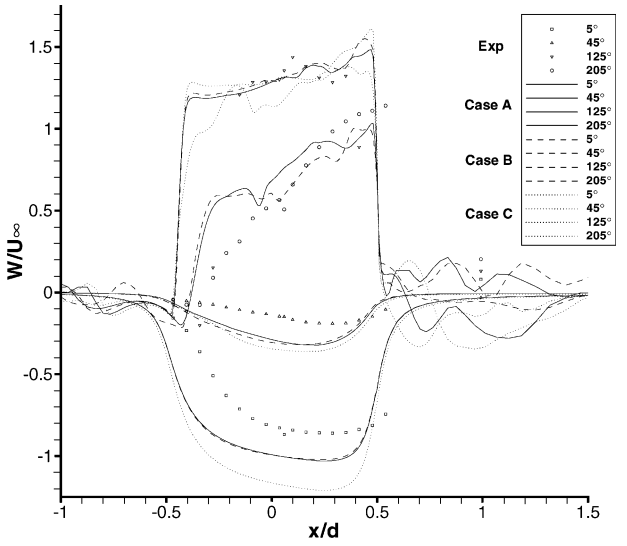

Fig. 5 Influence of the time step and actuator boundary condition on the phase-averaged values of w/U_∞ after two periods at $y/d = 0$, $z/\delta = 0.02$.

Table 4 Mesh size and turbulence modeling study

Computation designation	Mesh designation	Numerical method	Inflow boundary condition
LES-M1+F	Fine with inflow domain	LES	R[a]
LES-M1	Fine	LES	S[b]
LES-M2	Intermediate	LES	S
LES-M3	Coarse	LES	S
URANS-M3	Coarse	URANS+SA	S

[a]R, realistic boundary layer with turbulent shear stresses.
[b]S, steady RANS mean velocity profile.

Table 5 Computational parameters of the different cases

Computation designation	Time step, μs	Time steps per cycle	CPU time per cycle, h
LES-M1+F	0.5	13,333	57.6
LES-M1	0.5	13,333	55.2
LES-M2	1	6,667	14.7
LES-M3	2	3,333	1.3
URANS-M3	2	3,333	2

B. Comparison with Experiment

For a comparison of the results given next with those of the other workshop participants, readers can refer to the results summary of Rumsey et al.[40] Five computations have been performed in order to study the influence of the mesh size, the inflow boundary condition, and type of turbulence modeling (Table 4).

The case LES-M1+F is a LES with turbulent inflow boundary condition. The effect of this condition will be analyzed by comparing with the case LES-M1 (without fluctuations). The grid-resolution study is performed without inflow fluctuations with the cases LES-M1, LES-M2, and LES-M3 (see Table 2 for the grid definition). Finally, the turbulence modeling effects will be assessed by comparing the LES-M3 case with the URANS-M3 case.

Table 5 shows the time step used, the number of time steps per period, and the CPU time per period on a single NEC/SX6 processor. The time step is chosen in order to have a $\mathrm{CFL}_{\max}$ lower than 15 for all cases. This empirical criterion comes from our experience of LES (for example, see Ref. 35). It ensures a good compromise between computational cost and accuracy. The LES-M1+F and LES-M1 cases have been carried out on four processors with the parallel version of FLU3M. For all cases, a transient time equivalent to five periods was necessary to reach the periodic regime. After that transient, statistics were collected on eight periods.

1. *Inflow Boundary Condition*

For all cases, the inflow boundary condition is based on a steady RANS mean velocity profile. In the case LES-M1+F, a realistic turbulent inflow condition has been added. Numerically, this is achieved by the adjunction of a new block (with a spanwise width of $3d$) from which turbulent fluctuations are reintroduced at its entry (see Ref. 37 for more details). This domain is initialized with a previous flat-plate LES computation. On the lateral side, periodic boundary conditions are applied. By fixing the mean velocity profile to the RANS one, the temporal growth of the boundary layer is prevented. Figures 6 and 7 compare time-averaged longitudinal velocity and turbulent stresses profiles at the domain entry obtained both experimentally and numerically. For the computation of u^+ and z^+, the experimental data have been nondimensionalized by the RANS friction velocity. The mean skin-friction coefficient of the LES-M1+F is 2.52×10^{-3}, whereas 2.93×10^{-3} is expected for a standard incompressible experiment. This 14%

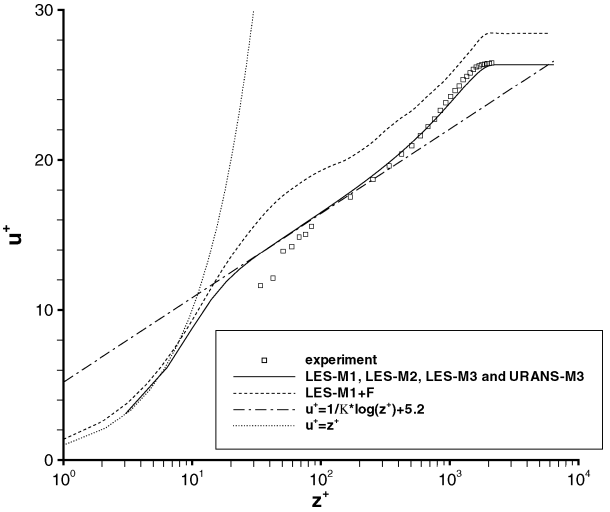

Fig. 6 Time-averaged velocity u/U_∞ in terms of law of the wall at $x/d = -8, y/d = 0$.

underestimation is a little more than the 10% error ordinary encountered in LES of boundary layers. The logarithmic zone of the longitudinal velocity profile is also too short in comparison with the RANS one.

Figure 7 shows that there are no fluctuations in the incoming flow for the simulations LES-M1, LES-M2, and LES-M3 as explained before. For URANS-M3, the turbulence model has been added as explained in Sec. III.A:

$$u_i' u_j' \rfloor_{\text{total}} = u_i' u_j' - \nu_t \left(\frac{\partial u_i}{\partial x_j} + \frac{\partial u_j}{\partial x_i} \right) - \frac{2}{3} k \delta_{ij} - \frac{2}{3} \nu_t \delta_{ij} \text{div} \boldsymbol{u} \qquad (5)$$

For LES-M1+F, the maximum of $u'u'/U_\infty^2$ is slightly underestimated (-11%), whereas for URANS-M3 this maximum is even lower (-76%). For $w'w'/U_\infty^2$, the LES-M1+F is in good agreement with the experiment, whereas the URANS overestimates it by 40%. For $u'w'/U_\infty^2$, the agreement with the experimental data is better for LES-M1+F than for URANS-M3 except for $z/\delta > 0.5$.

2. Analysis of Instantaneous Fields

Figure 8 shows the isovalue of the Q-criterion colored with the streamwise vorticity ω_x for the five cases. Even if more powerful criteria for vortex identification in a turbulent flow exist (e.g., λ_2), the Q-criterion is a good compromise between computational cost and quality. A vortex is characterized by a second invariant of the stress tensor Q positive with Q defined as

$$Q = \frac{1}{2}(\Omega_{ij}\Omega_{ij} - S_{ij}S_{ij}) = -\frac{1}{2}\frac{\partial u_i}{\partial x_j}\frac{\partial u_j}{\partial x_i} \qquad (6)$$

Q is nondimensionalized by U_∞^2/d^2. For LES-M1+F, turbulent structures characteristic of a boundary layer can be seen upstream of the jet because of the realistic inflow boundary condition. Nevertheless, a careful analysis does not reveal any change in the jet flow structure when compared to LES-M1. A visual comparison of results on LES-M1, LES-M2, and LES-M3 grids shows that when the grid is coarsened the number and the size of the ring vortices dramatically decrease. This is not surprising because LES is not supposed to achieve grid convergence because (see Ref. 31 for details), without prefiltering, refining the grid increases the spectral content of the solution. Nevertheless, if the filter width is kept constant by filtering the solution at every time step, grid convergence could be achieved, but it is not done in practice.

The comparison of cases LES-M3 and URANS-M3 enables one to evaluate the effect of the turbulence modeling. The structure of both flows is very different: the ring vortices on the windward side of the jet have disappeared in URANS-M3, whereas six ring vortices are visible in the LES-M3. The horseshoe vortex just upstream of the

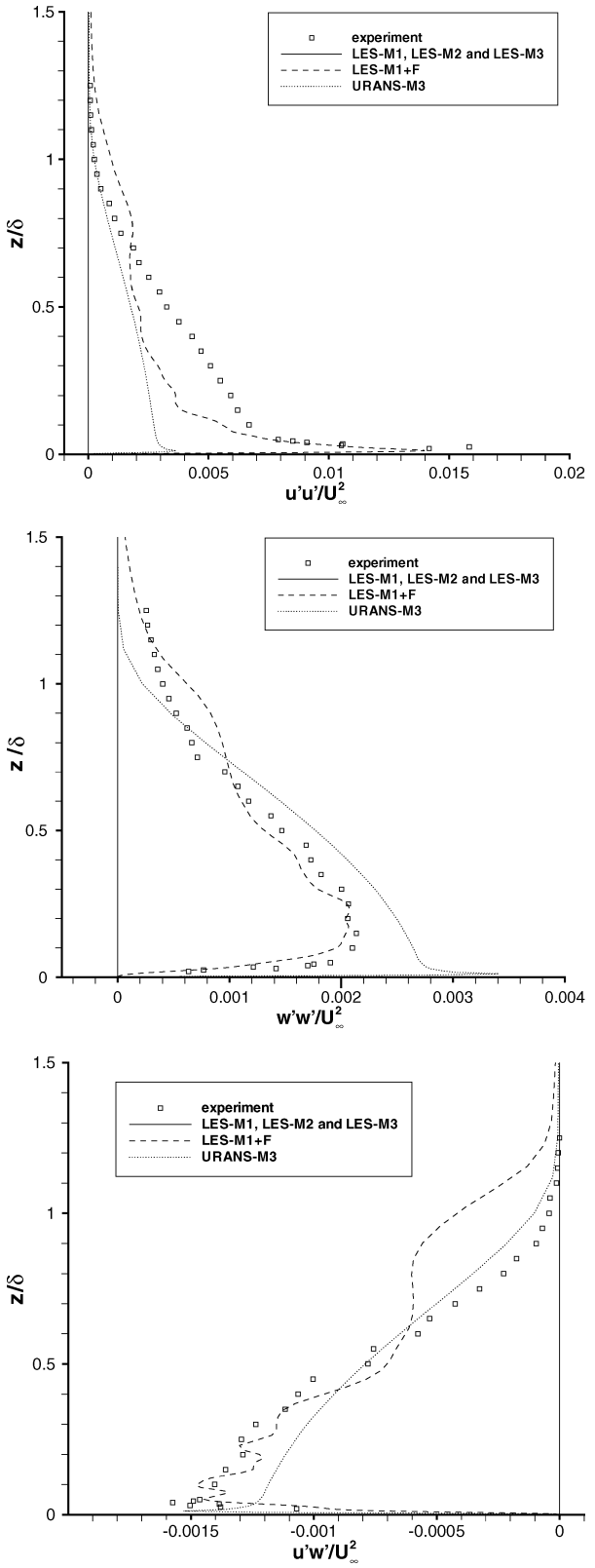

Fig. 7 Time-averaged normal and shear stresses $u'u'/U_\infty^2$, $w'w'/U_\infty^2$, and $u'w'/U_\infty^2$ at $x/d = -8, y/d = 0$.

jet is smaller in URANS than in LES, and the wall vortices below the jet have also disappeared. Nevertheless, the main structure of a jet in a crossflow, namely, a counter-rotating vortex pair (CVP) aligned with the streamwise direction, is still present.

3. Time-Averaged u/U_∞ Velocity Flowfield in the Plane $x/d = 0.25$

Figure 9 shows the time-averaged flowfield of u/U_∞ in the plane $x/d = 0.25$. A dome of low-momentum fluid, centered on $y/d = 0$

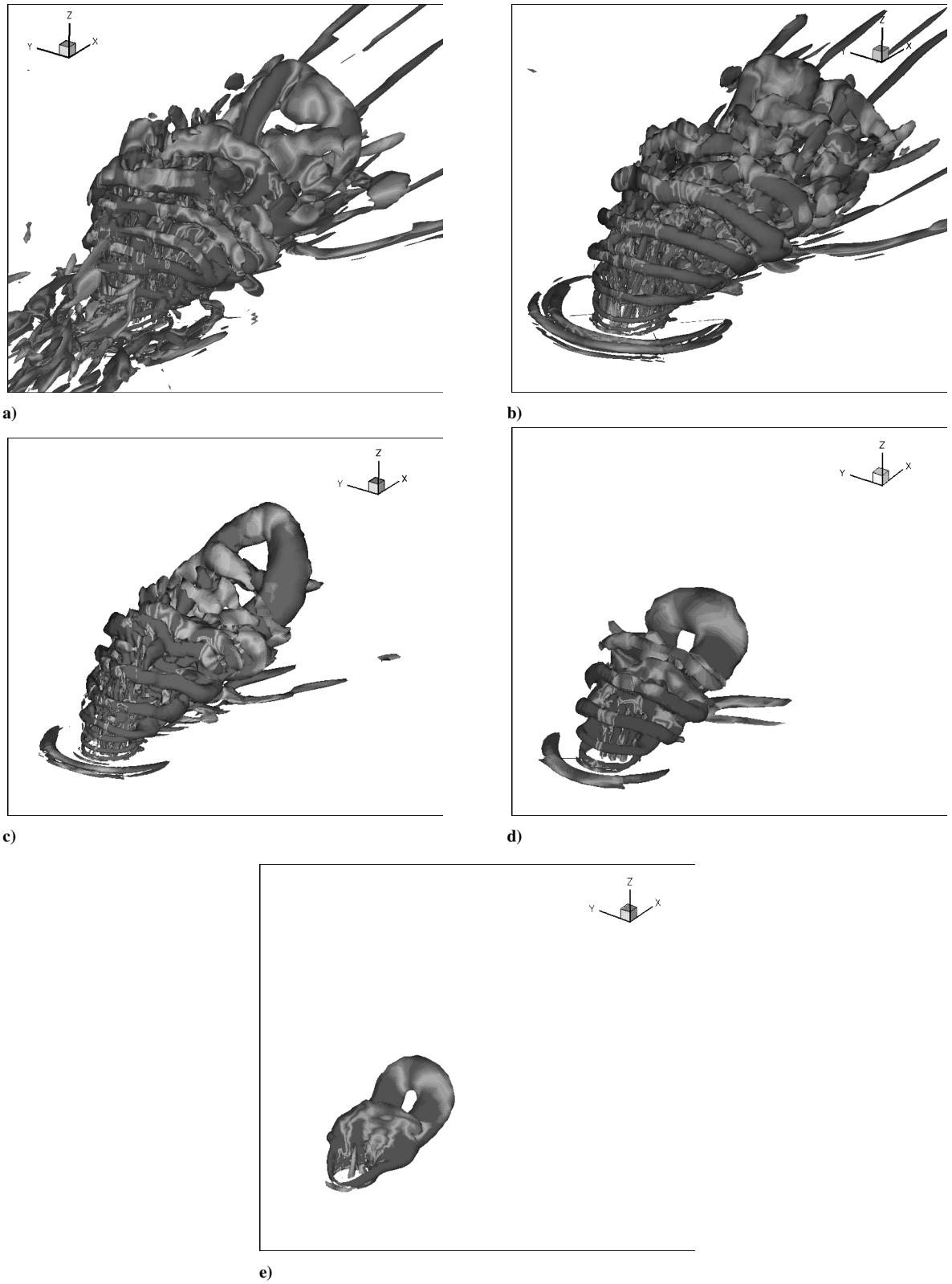

Fig. 8 Q-criterion isovalue $Q = 0.2$ colored with streamwise vorticity at blowing maximum for a) LES-M1 + F, b) LES-M1, c) LES-M2, d) LES-M3, and e) URANS-M3.

and of spanwise extent $0.5d$, is visible in all figures. The "kidney-shape" region, characteristic of a steady jet in a crossflow, is also retrieved near $z/d = 1$. For synthetic jets, this kidney shape is visible only near the orifice as reported by Zaman and Milanovic[18] in contrast with a steady jet where this velocity overshoot region persists farther downstream. At $x/d = 0.25$, the kidney-shape region is split into two parts on each side of the jet. The size of these two regions decreases with the coarsening of the mesh. The effect of the turbulence modeling can be seen by comparing the LES-M3 and URANS-M3 cases in Fig. 9. The dome of URANS-M3 has a lower spanwise extent than LES-M3, and the kidney zone has disappeared. The contours of the low-momentum dome are observed to be smoothed by URANS. In this plane, the ratio ν_t/ν has a maximum value of 114 for the URANS-M3 case, compared with 4 for the LES-M3 case. This smoothing is therefore caused by a higher physical dissipation with URANS modeling. By comparing

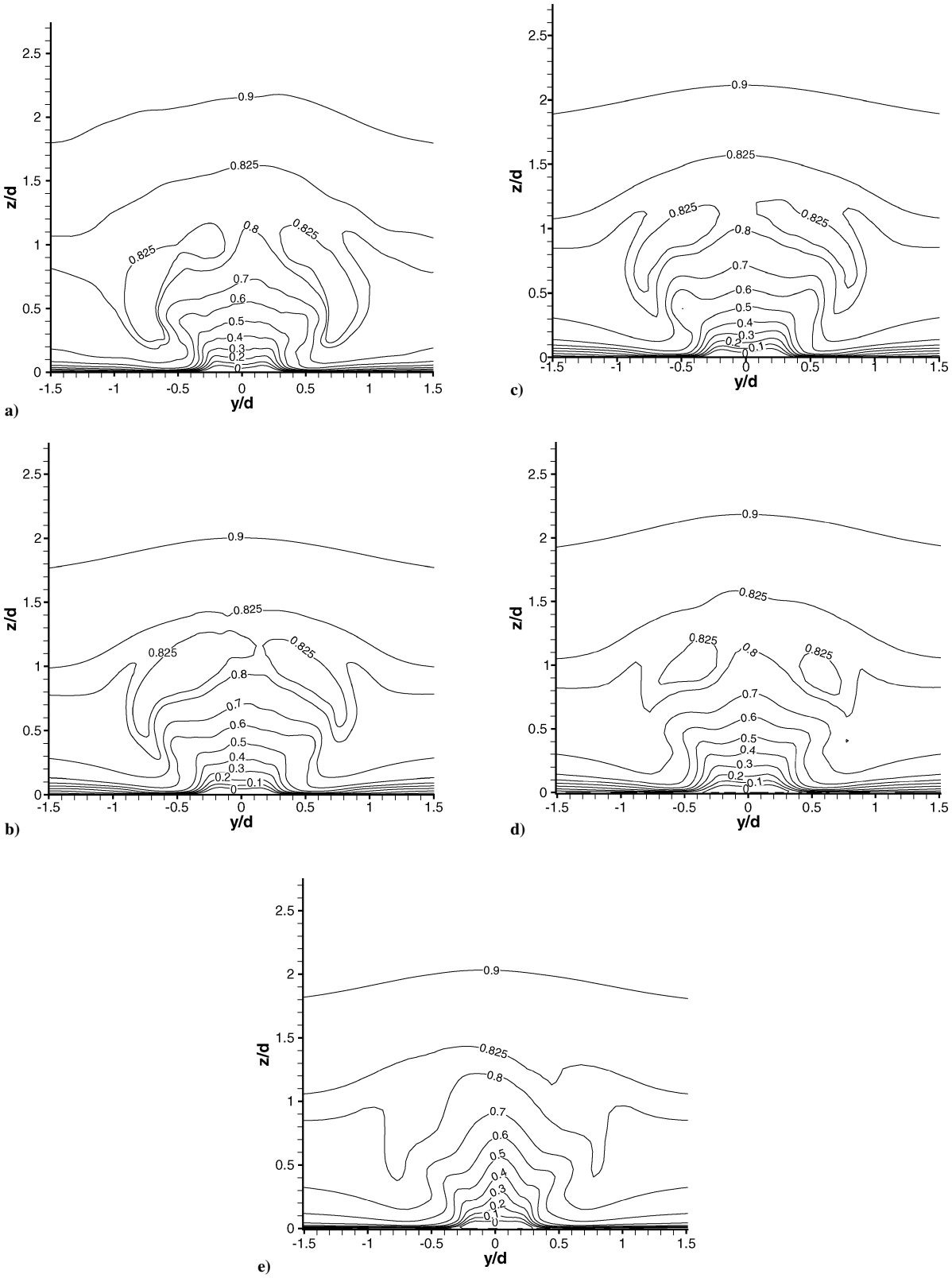

Fig. 9 Time-averaged u/U_∞ velocity flowfield in the plane $x/d = 0.25$ for a) LES-M1+F, b) LES-M1, c) LES-M2, d) LES-M3, and e) URANS-M3.

the LES-M1+F and LES-M1 cases, one can ascertain that with the turbulent inflow condition the two parts of the kidney-shape region are lower, and the penetration of the low-momentum dome is higher.

4. Time-Averaged Longitudinal Vorticity ω_x in the Plane $x/d = 3$

Figure 10 presents the nondimensionalized time-averaged longitudinal vorticity ω_x in the plane $x/d = 3$. The same scale for ω_x has been applied in all figures for comparison. The CVP is clearly visible near $z/\delta = 0.9$. This flow structure is the main feature of a jet in a crossflow and dominates downstream of the interaction. The CVP is more visible in this time-averaged flowfield that in the instantaneous fields of Fig. 8. The counter-rotating vortices below the main CVP are called wall vortices. Their vorticity signs are opposite to the CVP. Because of the low velocity ratio, the near-wall fluid is entrained by the main CVP and rolls up to form the wall vortices. It

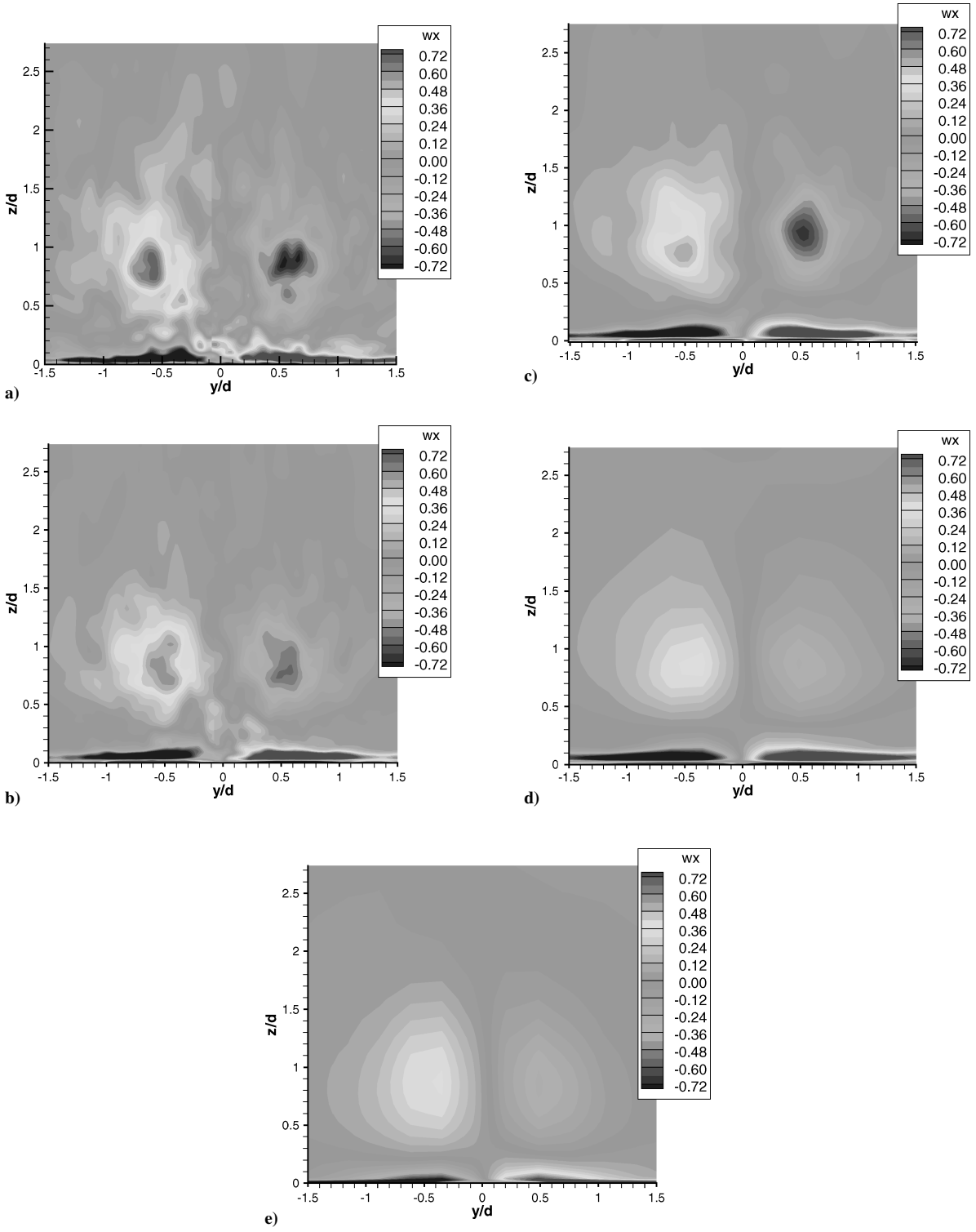

Fig. 10 Time-averaged longitudinal vorticity ω_x flowfield in the plane $x/d = 3$ for a) LES-M1+F, b) LES-M1, c) LES-M2, d) LES-M3, and e) URANS-M3.

can be seen that the wall vortices have a higher longitudinal vorticity than the CVP.

The comparison of the LES cases shows that the vorticity ω_x in the CVP decreases drastically when the mesh size is increased. The vorticity of the LES-M1 case is twice as high as the LES-M3 case. No modeling influence can be highlighted by examining the cases LES-M3 and URANS-M3, which have the same mean longitudinal vorticity in the CVP. Consequently, the grid resolution is the predominant parameter for the transport of these structures.

5. Temporal Evolution of the Velocity Components in the Orifice

Figure 11 shows the phase evolution of u, v, and w at a point near the orifice center. For u, the agreement with the experiment is better for the LES-M1+F case than for the other ones, in particular for phases smaller than 50 deg and larger than 280 deg, which correspond to the suction phase. In ejection phases, the error is larger with the coarsest grids (LES-M2, LES-M3, URANS-M3) independently of the modeling. As expected, the LES results are more noisy with the fine mesh than with the coarse one.

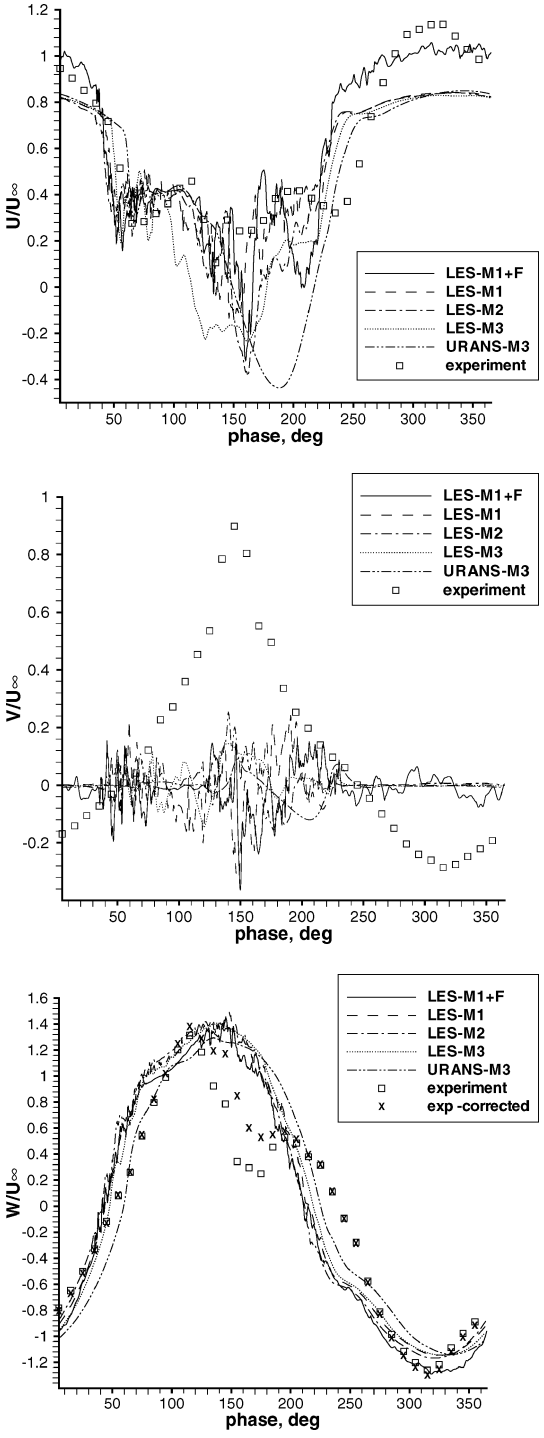

Fig. 11 Phase evolution of u/U_∞, v/U_∞, and w/U_∞ near the orifice's center ($x/d = -0.03$, $y/d = 0$, and $z/\delta = 0.02$).

The phase evolution of w shows that the phase synchronization between computations and the experiment is correct. The blowing maximum is reached at the phase 150 deg. As pointed out by Rumsey et al.[40] in the summary of the workshop results, all of the simulations cases predicted a near-zero spanwise velocity, whereas for the experiment v is near U_∞ at phase 150 deg. This can explain why there is a "dip" near the same phase on the w-velocity evolution. All of the other workshop participants have also found that $v \approx 0$ in the symmetry plane. Considering that the experimental station is located in the symmetry plane, the expected averaged spanwise velocity is supposed to be zero. This experimental bias could be explained by a nonvertical piston displacement.

In an attempt to anticipate the effects of a redistribution of the spanwise velocity component in the vertical plane, a possible correction of the vertical velocity has been proposed independently from NASA.

First we consider an x-axis rotation of the coordinate system in order to have $v = 0$. This implies that u is not modified. The new vertical velocity w_2/U_∞ is

$$w_2/U_\infty = \sqrt{(v/U_\infty)^2 + (w/U_\infty)^2} \tag{7}$$

The kinematic energy is not modified by the rotation. Moreover, it is observed in the velocity profile (Fig. 11) that v/U_∞ tends asymptotically toward 0.03 for $z/\delta > 0.7$ mm. And so Eq. (7) can be modified to ensure that w_2 tends toward zero for $z \to \infty$:

$$w_2/U_\infty = \sqrt{(v/U_\infty - 0.03)^2 + (w/U_\infty)^2} \qquad \text{for} \qquad w/U_\infty \geq 0 \tag{8}$$

$$w_2/U_\infty = -\sqrt{(v/U_\infty - 0.03)^2 + (w/U_\infty)^2} \qquad \text{for} \qquad w/U_\infty < 0 \tag{9}$$

As can be seen in Fig. 11, the dip in the w-velocity evolution is lower, and the agreement with all simulation cases is better. In the following, both w and w_2 are represented in the figures. The w_2 velocity is labeled "exp-corrected."

6. *Time-Averaged Velocities Profiles Downstream from the Jet*

Figure 12 presents profiles of the three velocity components at $x/d = 1$ in the symmetry plane $y/d = 0$. At this station, all simulations underestimate the longitudinal velocity deficit for $z/\delta < 0.2$. Such an underestimation was also observed in a NASA computation using the URANS method with the SA model on a finer grid than M3 (3.9×10^6 cells). Physically, this velocity deficit is caused by the blockage effect of the jet. Globally, on these profiles, the LES behavior is superior to the URANS one, and, in particular, the LES-M1+F is the closest to the experimental reference.

Concerning the w velocity, all simulations overpredict the first maximum near $z/\delta = 0.1$ and underpredict the second one near $z/\delta = 0.4$. Nevertheless, the proposed correction has a large influence on the first peak, and all results are located between the experiment and its possible correction. Therefore, the discrepancy on the first maximum might be partly caused by the asymmetry of the experimental data. The second peak is not modified by the correction. From a physical point of view, the first peak corresponds to the suction induced by the CVP, and the second one is in the jet core. The agreement on the two peaks becomes better downstream (Fig. 13).

The study of the effect of the mesh size shows that LES-M1, LES-M2, and LES-M3 cases are very close. The URANS-M3 case underestimates the w velocity in the jet core (second peak) in comparison with the case LES-M3 because of its higher level of dissipation.

Figure 13 presents the same velocities profiles $1d$ downstream. Both the longitudinal and vertical velocities profiles show that all simulations compare favorably with the experiments. At this station, the relaxation of the boundary layer in the near-wall region is well taken into account by all simulations and, in particular, by the LES-M1+F one. When compared to the preceding station, the amplitude of the two vertical velocity peaks is seen to decrease because of the jet momentum dissipation for the second peak and of the decay of the CVP circulation after $x/d = 0.5$ for the first peak. The first maximum is very well predicted by the LES-M1+F case, whereas the second one is somewhat overestimated. The w velocity is only slightly modified by the correction of the experimental data near the wall. As expected, the spurious asymmetry of the transverse velocity component is not represented by the computations. No significant grid dependence is noticed by comparing LES-M_x cases. The use of the realistic inflow condition is shown to globally improve the results on u- and w-velocity profiles.

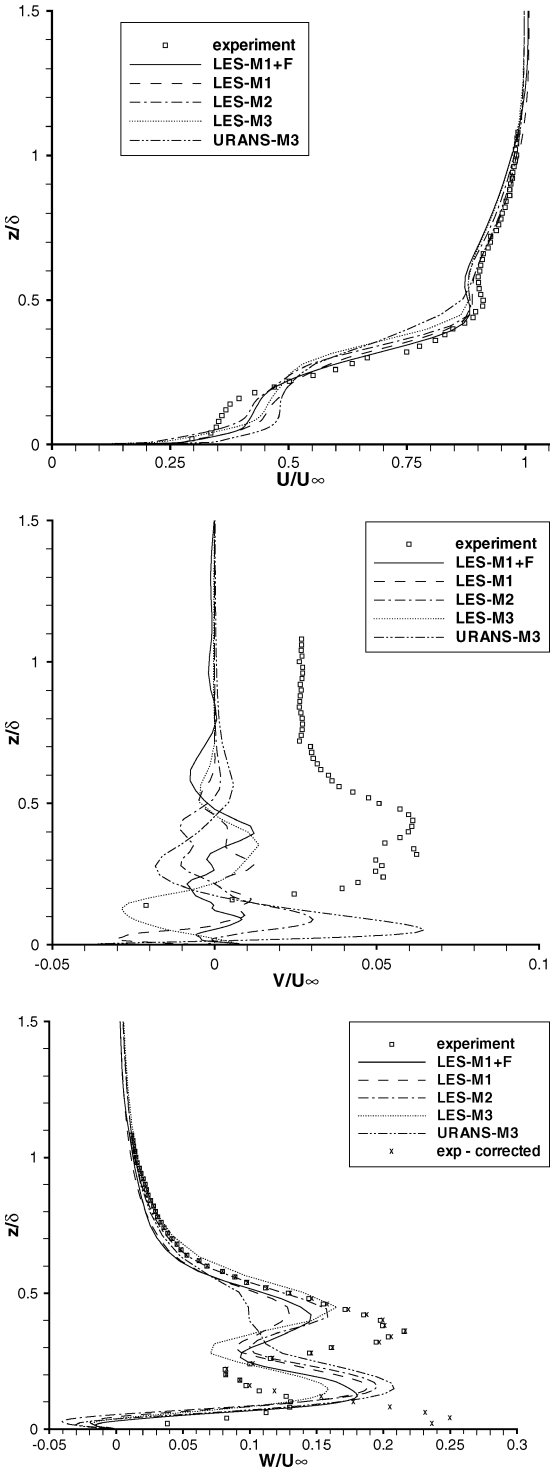

Fig. 12 Time-averaged velocities u/U_∞, v/U_∞, and w/U_∞ at $x/d = 1$, $y/d = 0$.

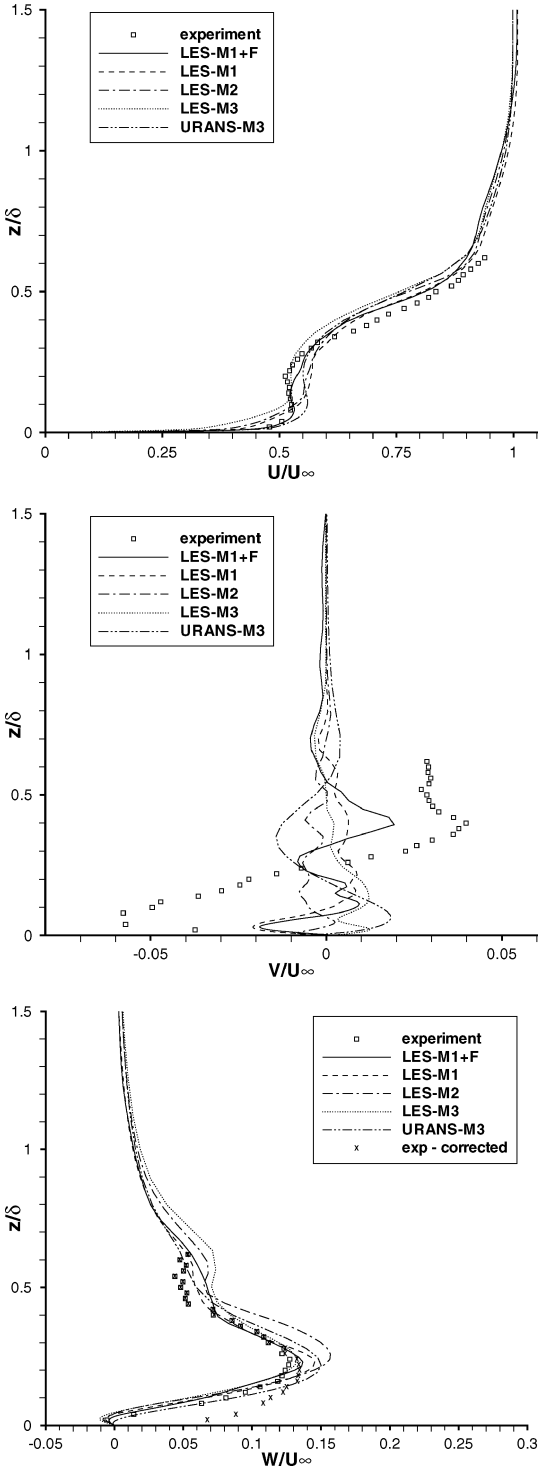

Fig. 13 Time-averaged velocities u/U_∞, v/U_∞, and w/U_∞ at $x/d = 2$, $y/d = 0$.

7. Phase-Averaged Velocities Profiles Downstream from the Jet

Figure 14 gives the u/U_∞-velocity profiles for three phases during blowing, which are both the most interesting and the most challenging parts of the synthetic jet cycle. The maximum blowing is for the phase 140 deg. The three presented phases exhibit the same features. The first maximum near $z/\delta = 0.1$ is caused by the blockage effect of the jet: the fluid accelerates to skirt round the jet, as for a cylinder in a crossflow. The minimum near $z/\delta = 0.25$ is in the core of the jet, which has a lower u velocity because of the jet bending. The second peak near $z/\delta = 0.5$ is located in the high-momentum region with a kidney shape, which is classically observed for steady jets in crossflows.[5]

Concerning the phase 120 deg, all of the computations agree well with one another, but an underestimation of the amplitude below $z/\delta = 0.2$ is observed. The URANS-M3 case surprisingly gives a better result for the first maximum but underpredicts the second one unlike the LES-M1+F, LES-M1, and LES-M2 cases for which the agreement with the experimental data is quite satisfactory. Looking at the other phases, the first peak is always overestimated by the URANS-M3 case. This might be related to the lower spanwise extent of the low-momentum dome observed in Fig. 9, which shows that the blockage effect is less pronounced in this simulation. The LES-M_x cases are in good agreement with one another on the first maximum. This confirms that the coarsest grid is sufficient to take into account the main features of the jet. It can be observed on

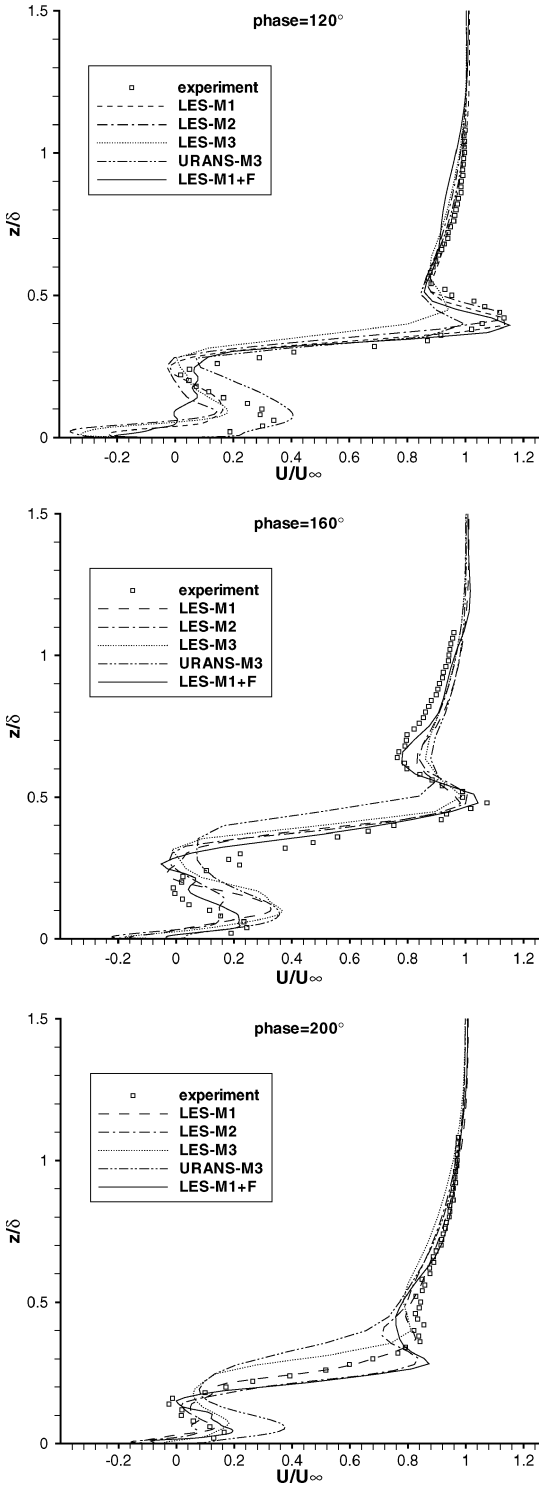

Fig. 14 Phase-averaged velocity u/U_∞ at phase 120, 160, and 200 deg and at $x/d = 1$, $y/d = 0$.

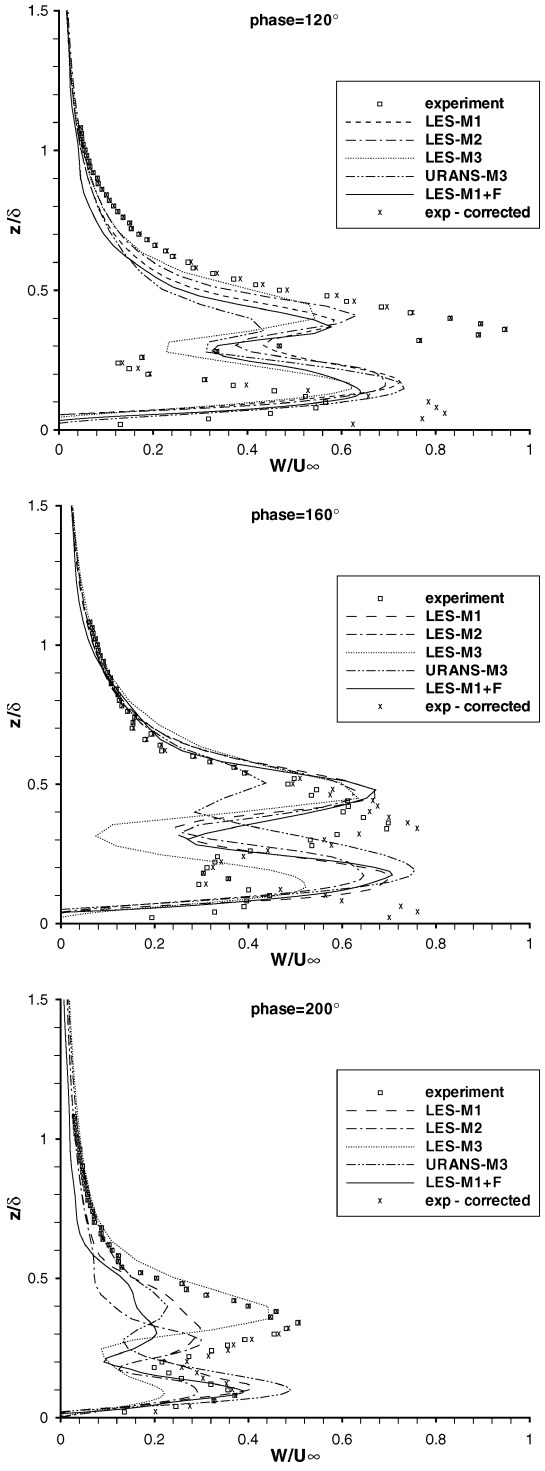

Fig. 15 Phase-averaged velocity w/U_∞ at phase 120, 160, and 200 deg and at $x/d = 1$, $y/d = 0$.

phases 160 and 200 deg that the two maxima at $z/\delta = 0.05$ and 0.4 are well predicted by all simulations. The LES computation on the coarse grid (LES-M3) is closer to the experiment than the URANS one. The comparison of LES-M_x simulations shows that the mesh refinement slightly improves the accuracy on the second peak of phase 120 deg and the first peak of phase 160 deg. The use of realistic inflow condition generally improves the results accuracy on the extrema of the u-velocity profile.

Figure 15 displays the w/U_∞-velocity profiles for the same phases as the preceding figure. At phase 120 deg, one can notice that all computations predict a too high velocity for the first maximum at $z/\delta = 0.1$ and that this peak is shifted toward $z/\delta = 0.15$. Once more, all simulations ranges between the experiment and its possible correction. The second maxima at $z/\delta = 0.35$ is underestimated by all computations in particular by URANS-M3 like for the time-averaged w-velocity profile of Fig. 12. Concerning the phase 160 deg, the agreement on the amplitude of the maxima is better with the corrected experimental data, but the two peaks are closer to the wall like for the phase 120 deg. This is caused by the dip observed on the w/U_∞ velocity of Fig. 11. The jet velocity is lower than in the simulation, and consequently the jet bending is higher. For phase 200 deg, the fine grid represents accurately the first maximum at $z/\delta = 0.1$. All of the simulations underestimate the second one at $z/\delta = 0.35$. The URANS-M3 simulation gives a too low amplitude of the second peak for all phases because of its higher dissipation.

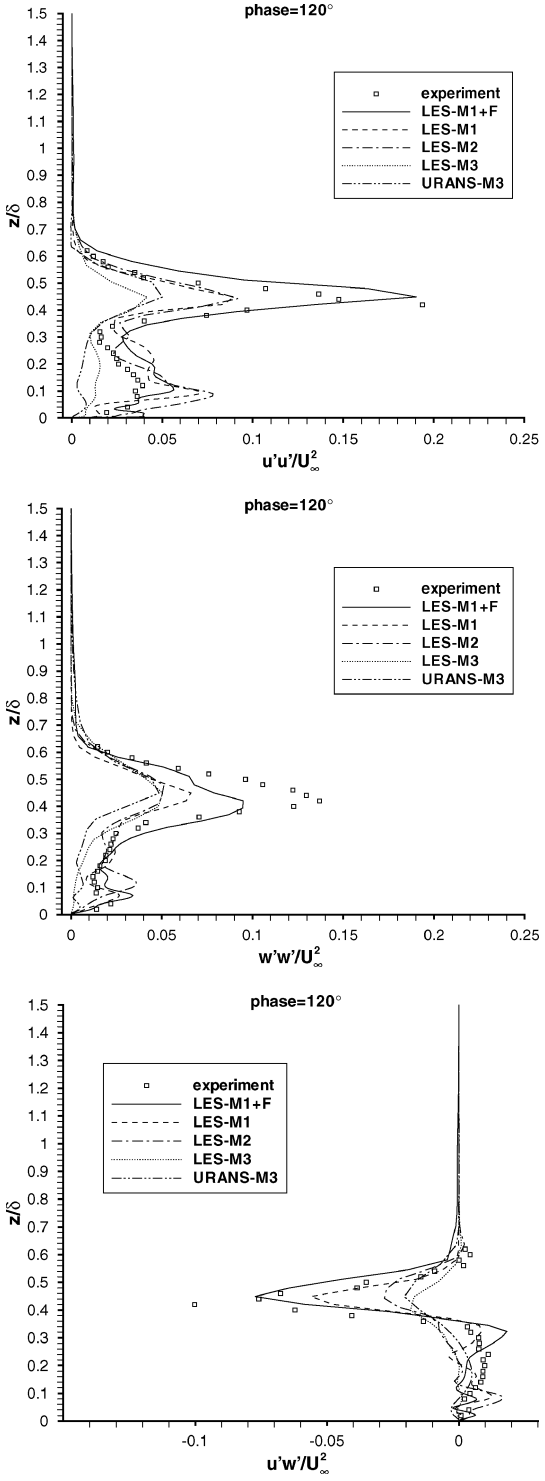

Fig. 16 Phase-averaged normal and shear stresses $u'u'/U_\infty^2$, $w'w'/U_\infty^2$, and $u'w'/U_\infty^2$ at phase 120 deg and $x/d = 2$, $y/d = 0$.

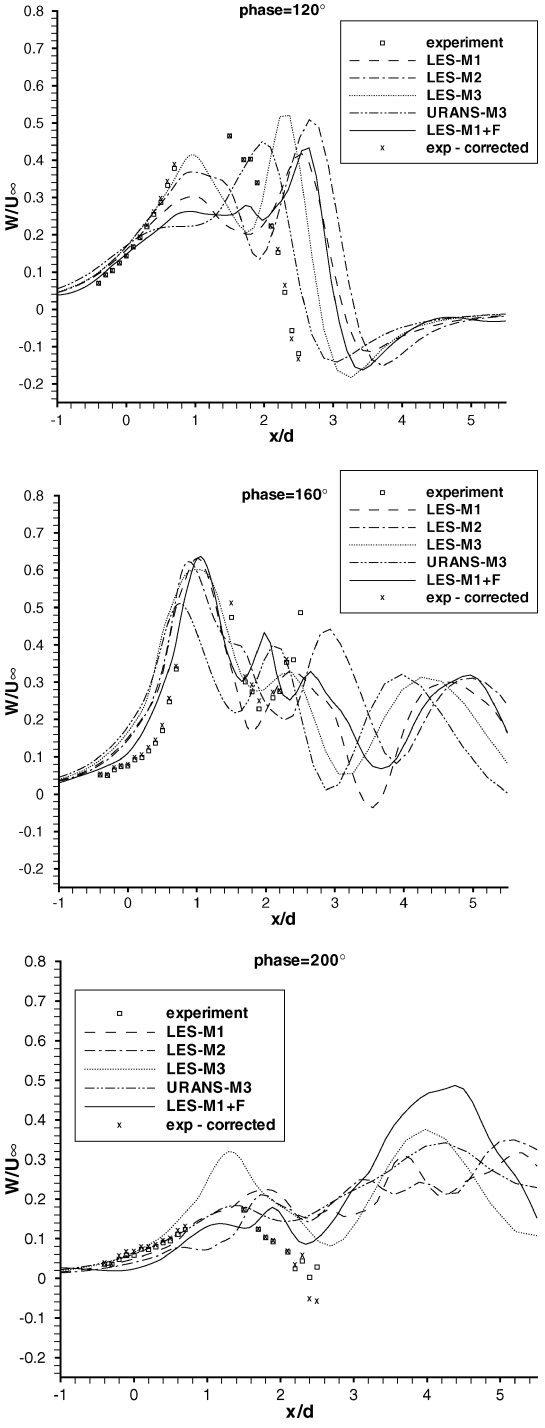

Fig. 17 Phase-averaged velocity w/U_∞ at phase 120, 160, and 200 deg and at $y/d = 0$, $z/\delta = 0.5$.

8. Phase-Averaged Turbulent Stresses Profiles Downstream from the Jet

Figure 16 displays the turbulent stresses $u'u'$, $w'w'$, and $u'w'$ profiles at phase 120 deg, a short time before the blowing maximum. The maximum of these stresses near $z/\delta = 0.5$ is located in the CVP just below the jet core.

One can notice that the second maxima of the longitudinal velocity fluctuation u' is underestimated by all simulations with the exception of LES-M1+F, which is in very good agreement with the experiment. For the $w'w'$ normal stress profile, the maximum is underpredicted by all simulations, but its position is correctly assessed. Concerning the cross stresses $u'w'$, both the grid-resolution increase and the turbulent inflow fluctuation addition have a favorable impact on the results, the first being the most efficient. On the contrary, for u' the main source of improvement is caused by the realistic inflow condition. Moreover, for the three turbulent stresses profiles the comparisons of the LES-M3 case with the URANS-M3 case demonstrate that there is no improvement when using LES turbulence modeling on too coarse grids.

9. Longitudinal Evolution in the Middle of the Boundary Layer

Figure 17 displays the longitudinal evolution of the vertical velocity w/U_∞ in the middle of the boundary layer for three phases during blowing. The first peak near $x/d = 0$ is located in the jet core. The other peaks whose number are growing between 120 and 200 deg correspond to wake vortices, which bring fluid from the wall vicinity into the CVP.

One can notice in the w-velocity profiles at phase 120 deg that LES computations predict two maxima, whereas only one is indicated by URANS-M3. In the experimental data, no second maxima downstream of the first one is visible. Nevertheless, because no experimental data are available between $x/d = 0.7$ and 1.5 and downstream of $x/d = 2.5$. it is not possible to draw some definitive conclusions on this point. Concerning the phase 160 deg, the first maxima at $x/d = 1$ is well predicted by all of the LES simulations, but the second maxima at $x/d = 2.5$ is on the contrary underestimated by all computations. For phase 200 deg, all of the simulations underestimate the first maximum near $x/d = 1$.

Globally, the vertical velocity acceleration with respect to the streamwise direction is correctly taken into account by all of the simulations.

V. Conclusions

A study of the interaction of a synthetic jet with a turbulent boundary layer has been performed to address the major numerical issues concerning the way such a device should be computed. The time-step study proves that the solution is not very sensitive in the range of the parameters studied. It has been shown that the interpolation of the actuator displacement does not improve the results, and a simpler boundary condition imposing a periodic motion with an amplitude evaluated with an incompressibility assumption was found sufficiently accurate.

Second, a study of the influence of the mesh size, turbulence modeling, and inflow boundary condition has been performed. All of the computations agree reasonably with the experimental data. The main source of discrepancies between computations and experiments is caused by a spurious spanwise component of velocity as large as U_∞ observed in the symmetry plane of the experiment.

Although the instantaneous and time-averaged flowfields have displayed a strong dependency of the results to the grid resolution in terms of ring vortices numbers and counter-rotating vortex pair circulation, the time-averaged and phase-averaged velocity profiles do not highlight such a dependency. Moreover, on these profiles the change of turbulence modeling from LES to URANS has a very limited effect on the coarsest grid. The unsteadiness of the velocity field is driven by the unsteadiness of the synthetic jet and not by the turbulence fluctuations. The turbulent structures such as vortex rings are second rate and do not significantly influence velocity profiles. Nevertheless, the observation of a nearly equivalent results quality of URANS and LES in this simple nonreactive and nonseparated flow cannot be extended directly to more complex flow for which LES is expected to be superior.

LES with a sufficiently refined grid improves turbulent stresses profiles prediction. A further improvement is obtained by adding a realistic inflow boundary layer. Unfortunately for the present analysis, the expected gain of the LES-M1+F simulation on the spectral content of the solution could not be highlighted because of the lack of this quantity in the experimental data set.

From an engineering point of view, the main conclusion of this paper is that a URANS computation is sufficient to simulate the mean dynamic of this synthetic jet.

From an academic point of view, only LES (and DNS) is believed to be able to give all of the turbulent structures of a synthetic jet in a crossflow, which are necessary for the understanding of the CVP formation mechanism in particular.

References

[1]Peterson, S. D., and Plesniak, M. W., "Evolution of Jets Emanating from Short Holes into Crossflow," *Journal of Fluid Mechanics*, Vol. 503, March 2004, pp. 57–91.

[2]Walters, D. K., and Leylek, J. H., "A Detailed Analysis of Film Cooling Physics: Part I—Streamwise Injection with Cylindrical Holes," *Journal of Turbomachinery*, Vol. 122, Jan 2000, pp. 102–112.

[3]Johari, H., Pacheco-Tougas, M., and Hermanson, J. C., "Penetration and Mixing of Fully Modulated Turbulent Jets in Crossflow," *AIAA Journal*, Vol. 37, No. 7, 1999, pp. 842–850.

[4]Kelso, R. M., Lim, T. T., and Perry, A. E., "An Experimental Study of Round Jets in Cross-Flow," *Journal of Fluid Mechanics*, Vol. 306, 1996, pp. 111–144.

[5]Haven, B. A., and Kurosaka, M.,"Kidney and Anti-Kidney Vortices in Crossflow Jets," *Journal of Fluid Mechanics*, Vol. 352, Dec. 1997, pp. 27–64.

[6]Cortelezzi, L., and Karagozian, A. R., "On the Formation of the Counter-Rotating Vortex Pair in Transverse Jets," *Journal of Fluid Mechanics*, Vol. 446, Nov. 2001, pp. 347–373.

[7]Camussi, R., Guj, G., and Stella, A., "Experimental Study of a Jet in a Crossflow at Very Low Reynolds Number," *Journal of Fluid Mechanics*, Vol. 454, March 2002, pp. 113–144.

[8]Marzouk, Y. M., and Ghoniem, A. F., "Mechanism of Streamwise Vorticity Formation in a Transverse Jet," AIAA Paper 2002-1063, Jan. 2002.

[9]Yuan, L. L., Street, R. L., and Ferziger, J. H., "Large-Eddy Simulation of a Round Jet in Crossflow," *Journal of Fluid Mechanics*, Vol. 379, Jan. 1999, pp. 71–104.

[10]Glezer, A., "The Formation of Vortex Rings," *Physics of Fluids*, Vol. 31, No. 12, 1988, pp. 3532–3542.

[11]Eroglu, A., and Breidenthal, R. E., "Structure, Penetration, and Mixing of Pulsed Jets in Crossflow," *AIAA Journal*, Vol. 39, No. 3, 2001, pp. 417–423.

[12]M'Closkey, R. T., King, J. M., Cortelezzi, L., and Karagozian, A. R., "The Actively Controlled Jet in Crossflow," *Journal of Fluid Mechanics*, Vol. 452, Feb. 2002, pp. 325–335.

[13]Seifert, A., Bachart, T., Koss, D., Shepshelovich, M., and Wygnanski, I., "Oscillatory Blowing: a Tool to Delay Boundary Layer Separation," *AIAA Journal*, Vol. 31, No. 11, 1993, pp. 2052–2060.

[14]Chen, Y., Liang, S., Aung, K., Glezer, A., and Lagoda, J., "Enhanced Mixing in a Simulated Combustor Using Synthetic Jet Actuators," AIAA Paper 99-0449, Jan. 1999.

[15]Smith, B. L., and Glezer, A., "Jet Vectoring Using Synthetic Jets," *Journal of Fluid Mechanics*, Vol. 458, May 2002, pp. 1–34.

[16]Schaeffler, N. W., "The Interaction of a Synthetic Jet and a Turbulent Boundary Layer," AIAA Paper 2003-643, Jan. 2003.

[17]Smith, D. R., "Interaction of a Synthetic Jet with a Crossflow Boundary Layer," *AIAA Journal*, Vol. 40, No. 11, 2002, pp. 2277–2288.

[18]Zaman, K. B. M. Q., and Milanovic, I. M., "Synthetic Jets in Cross-Flow. Part I: Round Jet," AIAA Paper 2003-3714, June 2003.

[19]Milanovic, I. M., and Zaman, K. B. M. Q., "Synthetic Jets in Cross-Flow. Part II: Jets from Orifices of Different Geometry," AIAA Paper 2003-3715, June 2003.

[20]Gordon, M., and Soria, J., "PIV Measurements of a Zero-Net-Mass-Flux Jet in Cross Flow," *Experiments in Fluids*, Vol. 33, No. 6, 2002, pp. 863–872.

[21]Narayanan, S., Barooah, P., and Cohen, J. M., "Experimental Study of the Coherent Structure Dynamics & Control of an Isolated Jet in Cross flow," AIAA Paper 2002-0272, Jan. 2002.

[22]Cui, J., Agarwal, R. K., and Cary, A. W., "Numerical Simulation of the Interaction of a Synthetic Jet with a Turbulent Boundary Layer," AIAA Paper 2003-3458, June 2003.

[23]Mittal, R., Rampunggoon, P., and Udaykumar, H. S., "Interaction of a Synthetic Jet with a Flat Plate Boundary Layer," AIAA Paper 2001-2773, June 2001.

[24]Lee, C. Y., and Goldstein, D. B., "Simulation of MEMS Suction and Blowing for Turbulent Boundary Layer Control," AIAA Paper 2002-2831, June 2002.

[25]Rizzetta, D. P., Visbal, M. R., and Stanek, J., "Numerical Investigation of Synthetic-Jet Flowfields," *AIAA Journal*, Vol. 37, No. 8, 1999, pp. 919–927.

[26]Schaeffler, N. W., and Jenkins, L. N., "The Isolated Synthetic Jet in Crossflow: a Benchmark for Flow Control Simulation," AIAA Paper 2004-2219, Jan. 2004.

[27]Hussain, A. K. M. F., and Reynolds, W. C., "The Mechanics of an Organized Wave in Turbulent Shear Flow," *Journal of Fluid Mechanics*, Vol. 41, 1970, pp. 241–258.

[28]Spalart, P. R., and Allmaras, S. R., "A One Equation Turbulence Model for Aerodynamics Flows," AIAA Paper 92-0439, Jan. 1992.

[29]Deck, S., Duveau, P., d'Espiney, P., and Guillen, P., "Development and Application of Spalart Allmaras One Equation Turbulence Model to Three-Dimensional Supersonic Complex Configurations," *Aerospace Science Technology*, Vol. 6, No. 3, 2002, pp. 171–183.

[30]Baldwin, B., and Barth, T. J., "A One Equation Turbulence Transport Model for High Reynolds Number Wall-Bounded flows," AIAA Paper 91-0610, Jan. 1991.

[31]Sagaut, P., *Large-Eddy Simulation for Incompressible Flows. An Introduction*, 2nd ed., Springer, Berlin, 2002.

[32]Vreman, A. W., "Direct and Large Eddy Simulation of the Compressible Turbulent Mixing Layer," Ph.D. Dissertation, Dept. of Applied Mechanics, Univ. of Twente, Twente, The Netherlands, Dec. 1995.

[33]Lenormand, E., Sagaut, P., Ta Phuoc, L., and Comte, P., "Subgrid-Scale Models for Large-Eddy Simulation of Compressible Wall Bounded Flows," *AIAA Journal*, Vol. 38, No. 8, 2000, pp. 1340–1350.

[34]Péchier, M., Guillen, P., and Gayzac, R., "Magnus Effect over Finned Projectiles," *Journal of Spacecrafts and Rockets*, Vol. 38, No. 4, 2001, pp. 542–549.

[35]Mary, I., and Sagaut, P., "LES of a Flow Around an Airfoil near Stall," *AIAA Journal*, Vol. 40, No. 6, 2002, pp. 1139–1145.

[36]Edwards, J. R., and Liou, M. S., "Low-Diffusion Flux-Splitting Methods for Flows at All Speeds," *AIAA Journal*, Vol. 36, No. 9, 1998, pp. 1610–1617.

[37]Sagaut, P., Garnier, G., Tromeur, E., Larchevêque, L., and Labourasse, E., "Turbulent Inflow Conditions for Large-Eddy Simulation of Compressible Wall Bounded Flows," *AIAA Journal*, Vol. 42, No. 3, 2004, pp. 469–477.

[38]Larchevêque, L., Sagaut, P., Lê, T.-H., and Comte, P., "Large-Eddy Simulation of a Compressible Flow in a Three-Dimensional Open Cavity at High Reynolds Number," *Journal of Fluid Mechanics*, Vol. 516, Oct. 2004, pp. 265–301.

[39]Deck, S., and Nguyen, A. T., "Unsteady Side Loads in a Thrust-Optimized Contour Nozzle at Hysteresis Regime," *AIAA Journal*, Vol. 42, No. 9, 2004, pp. 1878–1888.

[40]Rumsey, C. L., Gatski, T. B., Sellers, W. L., III, Vatsa, V. N., and Viken, S. A., "Summary of the 2004 CFD Validation Workshop on Synthetic Jets and Turbulent Separation Control," AIAA Paper 2004-2217, Jan. 2004.

C. Rumsey
Guest Editor